Introducing the Condor Array Telescope. II. Deep imaging observations of the edge-on spiral galaxy NGC 5907 and the NGC 5866 Group: yet another view of the iconic stellar stream

Kenneth M. Lanzetta,^{1*} Stefan Gromoll,² Michael M. Shara,³ Stephen Berg¹, James Garland,³ Evan Mancini,¹ David Valls-Gabaud,⁴ Frederick M. Walter,¹ and John K. Webb⁵

- ¹Department of Physics and Astronomy, Stony Brook University, Stony Brook, NY 11794-3800, USA
- ²Amazon Web Services, 410 Terry Ave. N, Seattle, WA 98109, USA
- ³Department of Astrophysics, American Museum of Natural History, Central Park West at 79th St., New York, NY 10024-5192, USA
- ⁴Observatoire de Paris, LERMA, CNRS, 61 Avenue de l'Observatoire, 75014, France
- ⁵Institute of Astronomy, University of Cambridge, Madingley Road, Cambridge CB3 0HA, United Kingdom

2 October 2023

ABSTRACT

We used the Condor Array Telescope to obtain deep imaging observations through the luminance filter of the entirety of the NGC 5866 Group, including a very extended region surrounding the galaxy NGC 5907 and its stellar stream. We find that the stellar stream consists of a single curved structure that stretches 220 kpc from a brighter eastern stream to a fainter western stream that bends to the north and then curls back toward the galaxy. This result runs contrary to a previous claim of a second loop of the stellar stream but is consistent with another previous description of the overall morphology of the stream. We further find that: (1) an extension of the western stream appears to bifurcate near its apex, (2) there is an apparent gap of \approx 6 kpc in the western stream due east of the galaxy, (3) contrary to a previous claim, there is no evidence of the remnant of a progenitor galaxy within the eastern stream, although (4) there are many other possible progenitor galaxies, (5) there is another structure that, if it is at the distance of the galaxy, stretches 240 kpc and contains two very large, very low-surface-brightness "patches" of emission, one of which was noted previously and another of which was not. We not the number and variety of stellar streams in the vicinity of NGC 5907 and the apparent gap in the western stream, which may be indicative of a dark subhalo or satellite in the vicinity of the galaxy.

Key words: Dwarf galaxies (416), Dwarf irregular galaxies (417), Galaxies (573), Galaxy groups (597), Galaxy interactions (600), Galaxy mergers (608), Galaxy photometry (611) Galaxy spurs (620), Giant galaxies (652), Interacting galaxies (802), Low surface brightness galaxies (940), Galaxy tails (2125)

1 INTRODUCTION

Over the past several years, the subject of low-surface-brightness imaging of astronomical sources has experienced a resurgence of interest, driven by new instrumentation capable of recording low surface brightnesses over wide fields of view. The edge-on spiral galaxy NGC 5907 has become a prime target of such observations. The galaxy was discovered by William Herschel in 1788 using an 18.7-inch (47.5 cm) reflecting telescope (Herschel 1789) and is a member of the NGC 5866 Group, which consists of at least the galaxies NGC 5866 (or M102), NGC 5879, and NGC 5907. The NGC 5866 Group is located near on the sky to the M101 Group and the M51 Group, and the redshifts of all three groups are similar, which suggests that they are all part of the same structure.

Observations of NGC 5907 in H I by Sancisi (1976) showed that the galaxy exhibits a pronounced warp, which was also observed

at optical wavelengths by van der Kruit (1979), Sasaki (1987), and Sackett et al. (1994). Subsequent observations of the galaxy at optical wavelengths by Shang et al. (1998) and Zheng et al. (1999) revealed a remarkable stellar stream forming a section of a loop surrounding the disk of the galaxy. The galaxy and the stellar stream were then observed again at optical wavelengths by Martínez-Delgado et al. (2010), who reported that the stellar stream comprised not one but two full loops surrounding the disk of the galaxy and proposed that both loops could be plausibly modeled by N-body simulations as the accretion of a dwarf satellite onto the disk of the galaxy. Because the configuration was so striking and unusual, this image of NGC 5907 by Martínez-Delgado et al. (2010) became the iconic image depicting the effects of tidal interactions between accreting dwarf satellites and spiral galaxies and is likely one of the most widely-recognized and influential images of any galaxy ever. The galaxy was then observed again by Laine et al. (2016) using the Suprime-Cam imager on the Subaru 8.2-m telescope through the Sloan g', r', and i' filters and

^{*} E-mail: Kenneth.Lanzetta@stonybrook.edu

using the Infrared Array Camera on the Spitzer telescope at 3.6 μ m; these observations detected only the first loop of the stellar stream.

The situation took another dramatic turn when van Dokkum et al. (2019) used the Dragonfly Telephoto Array (Abraham & van Dokkum 2014) to again observe the galaxy and the stellar stream at optical wavelengths. These observations (1) showed no evidence at all of the second loop of the stellar stream but instead (2) indicated that the stellar stream consists of a single curved structure that stretches 220 kpc, from the brighter "eastern stream" or the first loop identified by Shang et al. (1998) and Zheng et al. (1999), across the southern edge of the galaxy, to a fainter "western stream" that bends to the north. Results of van Dokkum et al. (2019) further indicated (3) a "density enhancement near the luminosity-weighted midpoint of the [eastern] stream," which they interpreted as the "likely remnant of a nearly disrupted progenitor galaxy," (4) that the configuration could be plausibly modeled by N-body simulations, (5) a new "linear" feature emanating from the eastern stream toward the east and terminating on a "patch" of emission (6) a tentative extension of the western stream to the northeast looping back south toward the disk, (7) a tentative continuation of the eastern stream looping back to the disk, and (8) a previously-uncataloged dwarf galaxy located just west of the eastern stream. Subsequent observations at optical wavelengths by Müller et al. (2019) and by Byun et al. (2022) likewise showed no evidence at all of the second loop, although these observations also did not detect the western stream or any of the other features reported by van Dokkum et al. (2019).

In the late winter and spring of 2022, we used the Condor Array Telescope (Lanzetta et al. 2023) to obtain deep imaging observations through the luminance filter of the entirety of the NGC 5866 Group, including a very extended region surrounding the galaxy NGC 5907 and its stellar stream. Our motivation was severalfold:

- to assess the technical capabilities and sensitivity of Condor in comparison with other telescopes optimized for low-surface-brightness imaging, which is especially relevant since NGC 5907 and its stellar stream have become something of a benchmark within the low-surface-brightness community;
- to confirm (or refute) the results of van Dokkum et al. (2019) and to weigh in on the apparent discrepancy between the results of van Dokkum et al. (2019) and the results of Martínez-Delgado et al. (2010);
- to search for new low-surface-brightness features in the vicinity of NGC 5907, potentially with greater sensitivity than any previous observations;
- to exploit the higher angular resolution of Condor with respect to Dragonfly to help constrain the nature of the various low-surfacebrightness features in the vicinity of NGC 5907;
- and to set low-surface-brightness features in the vicinity of NGC
 5907 into the broader context of the NGC 5866 Group.

Here we report results of these observations, which together constitute the deepest imaging observations of NGC 5907 and its stellar stream and of the NGC 5866 Group yet obtained. In what follows, we adopt for the galaxy NGC 5907 a heliocentric recession velocity $v = 665 \pm 1$ km s⁻¹ and redshift $z = 0.002218 \pm 0.000002$ (Springob et al. 2005) and a distance $d \approx 17$ Mpc (Tully et al. 2016).

2 OBSERVATIONS

Condor is an "array telescope" that consists of six apochromatic refracting telescopes of objective diameter 180 mm, each equipped with a large-format (9576 \times 6388 pix²), very low-read-noise (\approx

Table 1. Details of observations.

	J2	Exposure		
Pointing	R.A.	Dec	(h)	
Condor field 6089	15:05:34.03	+55:54:32.76	22.7	
Condor field 6090	15:20:24.74	+55:54:32.76	25.0	
Condor field 6183	14:58:03.86	+57:16:21.72	19.7	
Condor field 6184	15:13:32.90	+57:16:21.72	24.1	
Condor field 6185	15:29:01.94	+57:16:21.72	9.1	
NGC 5907	15:15:53.69	+56:19:43.86	21.4	

1.2 e⁻), very rapid-read-time (< 1 s) CMOS camera. Condor is optimized for measuring *both* point sources *and* extended, very low-surface-brightness features and in its normal mode of broad-band operation obtains observations of exposure time 60 s over dwell times spanning dozens or hundreds of hours. In this way, Condor builds up deep images while simultaneously monitoring tens or hundreds of thousands of point sources per field at a cadence of 60 s. Details of the motivation, configuration, and performance of the telescope are described by Lanzetta et al. (2023).

In the late winter and spring of 2022, we used Condor to obtain deep imaging observations through the luminance filter of the entirety of the NGC 5866 Group. The Condor images differ from the Dragonfly images of NGC 5907 in three significant ways: (1) they are of higher angular resolution (with a plate scale of 0.85 arcsec pix⁻¹ for Condor versus 2.8 arcsec pix⁻¹ for Dragonfly), (2) they extend over a wider field of view, and (3) they were obtained at a more rapid cadence. Here we consider only deep images formed from sums of the individual exposures, neglecting any temporal aspects of the observations; we defer consideration these other aspects of the observations until elsewhere. These observations targeted NGC 5907 and the NGC 5866 Group in six different pointings: five pointings to "Condor fields" and one pointing centered on NGC 5907. All observations were obtained with an individual exposure time of 60 s, and the telescope was dithered by a random offset of ≈ 15 arcmin between each exposure. Details of the observations are presented in Table 1, which for each pointing lists the International Celestial Reference System (ICRS) coordinates of the field center and the total exposure time. The total exposure time summed over the six pointings is 122 hr.

3 CONDOR DATA PIPELINE PROCESSING

We processed the observations described in § 2 through the Condor data pipeline. The data pipeline processing proceeds in several steps as follows:

- (i) Each science image is bias subtracted using a "master bias" image determined from a sequence of 500 zero-second exposures. The master bias image appropriate for a particular science image is typically obtained on the morning immediately preceding or following the acquisition of the science image.
- (ii) The width of the central region of the autocorrelation function and the average sky background level of each science image are measured and recorded. These values are used subsequently to assess the quality of the science images.

¹ "Condor fields" are set of fields with field centers that tile the entire sky with the Condor field of view, allowing for overlap.

- (iii) Each science image is field flattened and background subtracted. As described by Lanzetta et al. (2023), this involves dividing the science image by an appropriate "twilight flat image" (i.e. a sum of images of the sky obtained during dusk or dawn twilight), masking regions of the image surrounding detectable sources using NoiseChisel (Akhlaghi & Ichikawa 2015; Akhlaghi 2019), fitting the resulting quotient with a high-order (typically eighth-order) two-dimensional polynomial, and subtracting the resulting polynomial fit from the quotient. Because the source mask depends on the background, this procedure is iterated through convergence (which typically requires four iterations).
- (iv) Each science image is astrometrically calibrated. As described by Lanzetta et al. (2023), this involves fitting parameters of an affine transformation and a seventh-order geometric distortion polynomial in the TPV projection to pixel coordinates of sources detected in the image and celestial coordinates of sources contained in the Gaia DR3 catalog (Gaia Collaboration et al. 2017, 2018, 2021; Gaia Collaboration 2022). The astrometric calibrations exhibit systematic differences between the transformed pixel and celestial coordinates of ≤ 0.1 arcsec.
- (v) Each science image is processed using MaxiMask (Paillassa et al. 2020), which is a convolutional neural network that identifies contaminants in astronomical images, including cosmic-ray events and satellite trails. Pixels flagged by MaxiMask are excluded from the subsequent analysis. Each science image is also processed using MaxiTrack (Paillassa et al. 2020), which is a convolutional neural network that identifies images affected by tracking errors.
- (vi) For each science image, an additional pixel mask is constructed, identifying pixels that are found in the master bias image to exhibit significant effects of random telegraph noise (e.g. Chao et al. 2019). Pixels flagged in this way are excluded from the subsequent analysis.
- (vii) Each science image is photometrically calibrated. As described by Lanzetta et al. (2023), this involves comparing aperture photometry of sources detected in the image to Sloan g' magnitudes of sources contained in the Gaia DR3 catalog (Gaia Collaboration et al. 2017, 2018, 2021; Gaia Collaboration 2022). The resulting magnitude zero points are used subsequently to assess the quality of the science images. Note that this procedure scales the luminance images to Sloan g' magnitudes, although the luminance bandpass is actually roughly comparable to the sum of the Sloan g' and r' bandpasses. This introduces a color-dependent ambiguity in the photometric calibration, which for low-redshift galaxies amounts to ≈ 0.25 mag.
- (viii) Each science image is associated with an uncertainty image, which propagates the 1σ uncertainty appropriate for each pixel, starting from read noise and photon noise.
- (ix) Science images are rejected from the analysis based on (1) poor or impossible astrometric calibration (indicating clouds or obstruction by an observatory wall), (2) large width of the autocorrelation function (indicating out-of-focus images or poor seeing conditions), (3) high background (indicating substantial manmade or Moon light), (4) low sky transparency (indicating fog, haze, or clouds), or (5) significant tracking errors (indicating substantial wind buffeting).
- (x) The science images are then drizzled (Gonzaga et al. 2012) onto a common coordinate grid and coadded weighted for maximum sensitivity in the background-limited regime according to the uncertainty images.

The resulting coadded images are show in Figures 1 through 6, and a coadded mosaic of the six images of the entirety of the NGC 5866

Table 2. Image FWHM and sensitivities. Point-source sensitivities are 5σ , and surface-brightness sensitivities are 3σ over 10×10 arcsec² regions.

Pointing	FWHM (arcsec)	Point Source (mag)	Surface Brightness (mag arcsec ⁻²)
Condor field 6089	2.6	24.9	29.5
Condor field 6090	3.0	24.6	29.4
Condor field 6183	2.6	24.8	29.4
Condor field 6184	3.0	24.7	29.5
Condor field 6185	3.0	23.9	28.7
NGC 5907	2.1	25.2	29.6
mosaic	2.3	25.5	29.9

Group is shown in Figure 7. The measured point-source FWHM and point-source (5 σ) and surface-brightness (3 σ over 10 × 10 arcsec² regions) sensitivities of the various images (determined near the centers of the images) are presented in Table 2. Note that the FWHM of Table 2 include the combined effects of focus, seeing, tracking errors, and astrometric errors averaged over many images. Also note that the surface-brightness sensitivities of Table 2 are formal statistical values determined from the uncertainty images and neglect systematic uncertainties associated with field flattening, background subtraction, scattered starlight, and undetected faint sources. And finally note that the sensitivities of Table 2 do not scale in a simple way with exposure time. For a telescope like Condor that obtains observations spanning long dwell times, there will of course be significant variations in seeing, background, and sky transparency over the course of the (perhaps substantial) duration of the observations. So for this reason, exposure time alone is not a good indicator of the depth of an image.

4 ASSESSMENT OF FIELD FLATTENING AND BACKGROUND SUBTRACTION

Errors in field flattening and background subtraction can be significant sources of systematic uncertainties at low surface-brightness thresholds. Here we assess the field flattening and background subtraction of the images of Figure 1 through 7, concentrating on the mosaic image of Figure 7.

One possible assessment of errors in field flattening and background subtraction might be obtained by measuring fluctuations within randomly chosen apertures that by chance are devoid of detectable sources. But at the faint limits of the images of Figures 1 through 7, the sky is covered with faint sources (mostly background galaxies), at an incidence that exceeds 10 $\operatorname{arcmin}^{-2}$. Hence there are essentially *no* apertures as large as, say, $1 \times 1 \operatorname{arcmin}^2$ (or even $0.5 \times 0.5 \operatorname{arcmin}^2$) that are devoid of detectable sources.

Instead, we assess errors in field flattening and background subtraction by measuring the data covariance over "background" pixels of the images, i.e. pixels of the images that are *not* masked surrounding detectable sources using NoiseChisel (as described in § 3, enumerated point iii). On small spatial scales (i.e. on scales of a few pixels), we expect the images to be highly correlated due to the drizzling process used to coadd the images (as described in § 3, enumerated point x). But on larger spatial scales (i.e. on scales of tens, hundreds, or thousands of pixels), the images should ideally exhibit zero covariance, and any non-zero covariance must indicate large-spatial-scale undulations of the background, which could be due in part to errors in field flattening and background subtraction.

4 Lanzetta, Gromoll, Shara, et al.

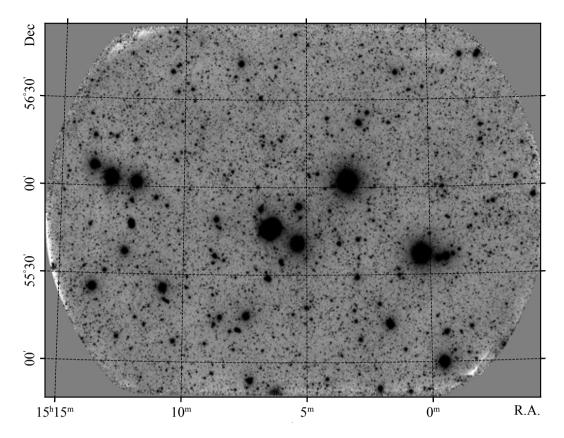


Figure 1. Coadded image of Condor field 6089. Image is smoothed by Gaussian kernel of FWHM = 2.5 pix. Total exposure time is 22.7 hr.

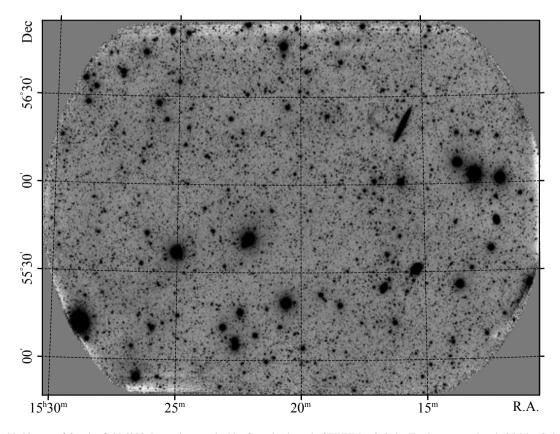


Figure 2. Coadded image of Condor field 6090. Image is smoothed by Gaussian kernel of FWHM = 2.5 pix. Total exposure time is 25.0 hr. Galaxy NGC 5907 is toward upper right of image.

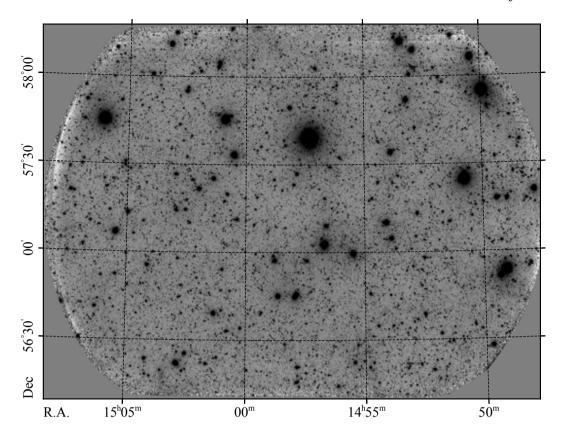


Figure 3. Coadded image of Condor field 6183. Image is smoothed by Gaussian kernel of FWHM = 2.5 pix. Total exposure time array is 19.7 hr.

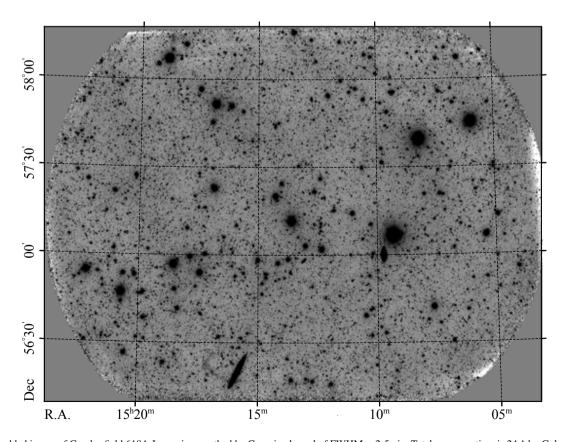


Figure 4. Coadded image of Condor field 6184. Image is smoothed by Gaussian kernel of FWHM = 2.5 pix. Total exposure time is 24.1 hr. Galaxy NGC 5907 is toward lower center of image.

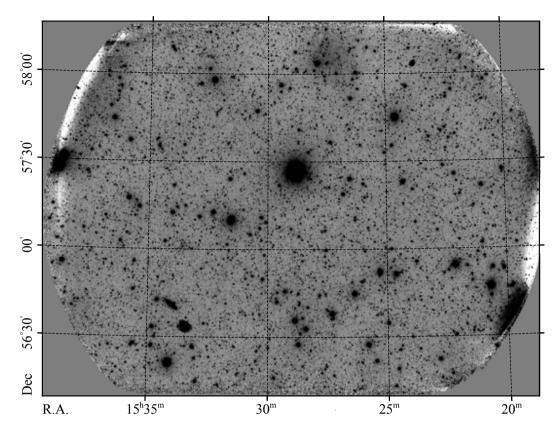


Figure 5. Coadded image of Condor field 6185. Image is smoothed by Gaussian kernel of FWHM = 2.5 pix. Total exposure time is 9.1 hr.

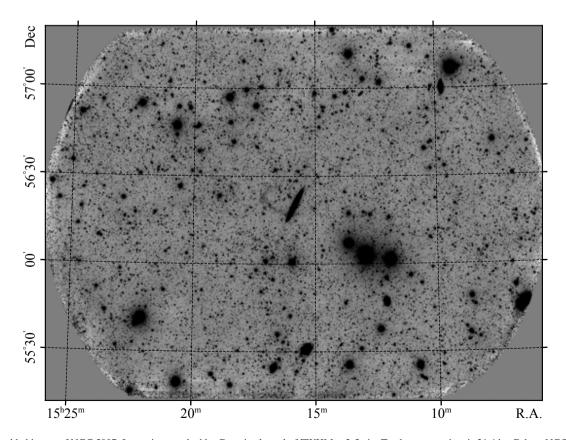


Figure 6. Coadded image of NGC 5907. Image is smoothed by Gaussian kernel of FWHM = 2.5 pix. Total exposure time is 21.4 hr. Galaxy NGC 5907 is near center of image.

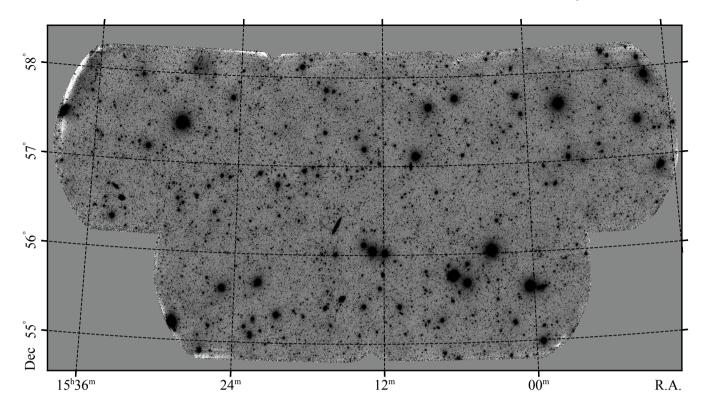


Figure 7. Coadded mosaic of the six images of the entirety of the NGC 5866 Group. Image is smoothed by Gaussian kernel of FWHM = 2.5 pix, and angular extent of image is $\approx 7.0 \times 3.5 \text{ deg}^2$. Total exposure time summed over all six pointings is 122 hr.

We consider some region of some image for which the uncertainty image over the background (i.e. unmasked) pixels is roughly constant. (This applies over the central regions of all of the images considered here.) The values of these pixels can be considered a random variable of zero mean and constant variance. We write the data covariance C_l^2 at some pixel lag l as

$$C_l^2 = \frac{1}{N-1} \sum_i x_i x_{i-l},\tag{1}$$

where the sum extends over the N background pixels of the region. The data covariance C_0^2 at zero pixel lag

$$C_0^2 = \frac{1}{N-1} \sum_i x_i^2 \tag{2}$$

is the pixel-to-pixel variance of the region. We further write the correlation coefficient ρ_l at pixel lag l as

$$\rho_l = \frac{C_l^2}{C_0^2}. (3)$$

Here we consider results obtained from a $5000 \times 5000 \text{ pix}^2$ region of the mosaic image of Figure 7 centered on NGC 5907, although similar results can of course be obtained using other regions of other images.

The distribution $\Phi(f_{\nu})$ of pixel-to-pixel energy fluxes f_{ν} of the background pixels of the mosaic region is shown by the blue curve in Figure 8. The pixel-to-pixel variance of the mosaic region is measured to be

$$C_0^2 = 1.569 \times 10^{-4} \,\mu\text{Jy}^2,$$
 (4)

while the median "statistical" variance σ_s^2 of the mosaic region

determined from the background pixels of the uncertainty is image is measured to be

$$\sigma_s^2 = 2.329 \times 10^{-4} \mu \text{Jy}^2. \tag{5}$$

The background pixels of the uncertainty image are indeed roughly constant over the mosaic region, and we use the median only to mitigate possible effects of deviant pixels. As expected, the pixel-to-pixel variance is *less* than the median variance determined from the uncertainty image, because the drizzling process used to coadd the images combines nearby pixels, which has the effect of "smoothing" the image and thus reducing the variance. We characterize the relationship between the pixel-to-pixel variance and the median variance determined from the uncertainty image by the ratio

$$r = \frac{C_0^2}{\sigma_s^2} = 0.674. \tag{6}$$

Gaussian distribution functions of standard deviations σ_s and $(C_0^2)^{1/2}$ are shown by the orange and green curves, respectively, in Figure 8. It is clear that a standard deviation σ_s is too wide to adequately describe the observed distribution (for the reasons described above) and that a standard deviation $(C_0^2)^{1/2}$ provides a better but still inadequate description of the observed distribution. Specifically, the observed distribution deviates from a Gaussian distribution function due to an extended tail of positive energy fluxes, which we attribute to sources missed by the masking procedure. A standard deviation 0.00995 μ Jy (determined by measuring the standard deviation of the observed distribution truncated at 0.025 μ Jy) is shown by the purple curve in Figure 8; this distribution function adequately describes the observed distribution except for the extended tail of positive energy fluxes. We conclude that pixel-to-pixel fluctuations of the mosaic region are well described by a

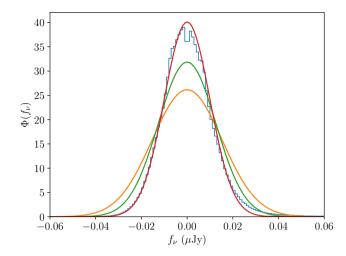


Figure 8. Distributions $\Phi(f_{\nu})$ of pixel-to-pixel energy fluxes f_{ν} of background pixels of mosaic region. Blue curve shows observed distribution, and orange, green, and purple curves show Gaussian distribution functions of standard deviations σ_s , $(C_0^2)^{1/2}$, and 0.00995 μ Jy, respectively.

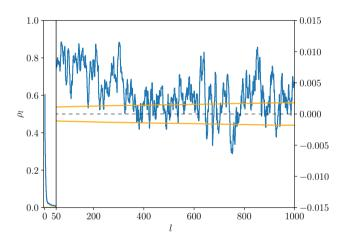


Figure 9. Correlation coefficient ρ_l (blue curves) together with positive and negative one standard deviation uncertainties (orange curves) of mosaic region for pixel lags over intervals l=0 through 50 (left panel and left scale) and l=50 to 1000 (right panel and right scale).

combination of a Gaussian distribution function of standard deviation $\approx 0.01~\mu Jy$ and an extended tail of positive energy fluxes due to sources missed by the masking procedure, which is prominent beyond ≈ 2.5 standard deviations.

The correlation coefficient ρ_l of the mosaic region for pixel lags over the interval l=0 through 1000 is shown in Figure 9. We note several results from Figure 9 as follows: (1) Neighboring pixels are highly correlated, with correlation coefficients ranging from $\rho_1=0.60$ for immediately adjacent neighbors to $\rho_5=0.16$ to $\rho_{10}=0.04$ to $\rho_{20}=0.02$. We attribute the strong correlation of neighboring pixels to the drizzling process. (2) Pixels remain correlated to a pixel lag of $l\approx 300$, with a correlation coefficient over the range l=50 to 300 of $\rho_l\approx 0.005$. We attribute the correlation of pixels at pixel lags l=50 to 300 to large-spatial-scale undulations of the background. And (3) pixels at pixel lags $l\gtrsim 300$ are uncorrelated or only weakly correlated.

We now consider the fluctuations attributable only to background

within an aperture that encompasses N pixels. If the N pixels are uncorrelated, then the variance σ_N^2 of the background within the aperture is

$$\sigma_N^2 = \sum_i C_0^2 = NC_0^2,\tag{7}$$

where the sum extends over the pixels that comprise the aperture. If the *N* pixels are correlated, then the variance is

$$\sigma_N^2 = \sum_i C_0^2 + \sum_i \sum_{j \neq i} C_l^2 \approx NC_0^2 + NC_0^2 2\pi \sum_{l=1}^{n/2} l\rho_l, \tag{8}$$

where the sums over i and j extend over the pixels that comprise the aperture and the sum over l extends over the diameter $n \sim N^{1/2}$ of the aperture. Expressing C_0^2 in terms of σ_s^2 and r via equation (6) then yields

$$\sigma_N^2 = \left(1 + 2\pi \sum_{l=1}^{n/2} l\rho_l\right) Nr\sigma_s^2.$$
 (9)

The corresponding relationship expressed in terms of a standard deviation rather than a variance is

$$\sigma_N = \left(1 + 2\pi \sum_{l=1}^{n/2} l\rho_l\right)^{1/2} N^{1/2} r^{1/2} \sigma_s. \tag{10}$$

Equation (10) provides the way to relate the formal statistical uncertainties of the uncertainty images (and hence the sensitives presented, e.g. in Table 2) to the actual uncertainties including effects of pixel-to-pixel correlations on small spatial scales (due to the drizzling process) and on large spatial scales (due to undulations of the background). Specifically, the ultimate effect of pixel-to-pixel correlations is to alter the standard deviation attributable only to background of an aperture that encompasses N pixels by a factor f_N given by

$$f_N = \left(1 + 2\pi \sum_{l=1}^{n/2} l\rho_l\right)^{1/2} r^{1/2} \tag{11}$$

with respect to the value

$$\sigma_N = N^{1/2} \sigma_s \tag{12}$$

that is obtained by considering the uncertainty images alone.

The resulting values of f_N measured for the mosaic region are shown (on a magnitude scale) versus angular scale θ (i.e. expressing diameter n in angular units) in Figure 10, using the correlation coefficient ρ_l from Figure 9 and the ratio r from equation (6). Fluctuations on single-pixel scales are *less* by a factor 0.82 (or -0.2 mag) than the value obtained by considering the uncertainty image alone due to the drizzling process. Fluctuations of the background over 0.5×0.5 and 1×1 arcmin² apertures exceed the values obtained by considering the uncertainty image alone by around 2.0 and 2.3 mag, respectively.

The values shown in Figure 10 represent *upper limits* to the errors in field flattening and background subtraction of the mosaic region, because fluctuations in the background also arise due to scattered starlight and to undetected faint sources (including the faint sources that make up the extended tail of positive energy fluxes of the distribution of pixel-to-pixel energy fluxes of the background pixels of the mosaic regions shown in Figure 8). Further, fluctuations in the background are not necessarily simply related to sensitivity; for example, a source of diameter 0.1 arcmin might be detected despite undulations in the background on scales of 1 arcmin. A detailed

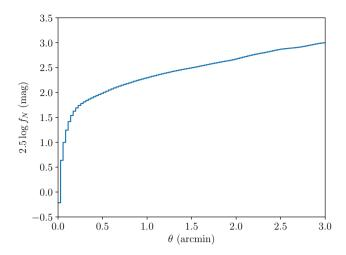


Figure 10. Factor f_N by which standard deviation of background is altered with respect to value obtained considering uncertainty images alone (on a magnitude scale) of the mosaic region versus angular scale θ .

accounting of all sources of fluctuations in the background will be described elsewhere.

5 CORRECTION FOR SCATTERED STARLIGHT

Although Condor exhibits a very clean point-spread function (PSF, Lanzetta et al. 2023), scattered starlight can be a significant source of systematic noise. Hence to fully exploit the sensitivity of the images described in § 3 to very low-surface-brightness features, it is necessary to correct for scattered starlight by (1) accurately determining the PSF on large angular scales and (2) using the resulting PSF to model and subtract the contributions of all stars within (and possibly even beyond) the field of view. Details of our method of PSF determination and subtraction will be described elsewhere, but here we present a brief summary of the procedures and results.

To determine the PSF, we compare a "data" image with a "model" image, where we take the model image to be the convolution of a "sky" image with a "PSF" image. We allow for the possibility that the model image (and hence the PSF image) is expressed on a finer grid than the data image (i.e. is "subsampled" with respect to the data image). We assume that the sky consists only of stars (i.e. we mask regions around galaxies and other non-stellar sources), and hence we take the sky image to be a sum of delta functions, where the locations of the delta functions (i.e. the locations of the stars) are taken as given. We then write the comparison between the data image and the model image as a linear least squares problem, and we solve the normal equations (e.g. Press et al. 2007) to minimize χ^2 with respect to some parameters. In particular, if the normalizations of the delta functions (i.e. the energy fluxes of the stars) are taken as given, then we solve the normal equations for the PSF image, or if the PSF image is taken as given, then we solve the normal equations for the energy fluxes of the stars. In practice, starting with any reasonable guess for the energy fluxes of the stars and iterating between solving for the PSF image and solving for the energy fluxes of the stars, the solution quickly converges to the desired simultaneous solution.

Our primary objective is to determine and subtract the PSF on large angular scales, and for this purpose, the limitations of a pixelbased approach are obvious: Near the core of the PSF, a fine pixel grid is both necessary (because the PSF exhibits rapid variations at small angles) and feasible (because observations of the PSF contain substantial signal at small angles). But moving outward from the core of the PSF, the same fine pixel grid becomes both unnecessary (because the PSF exhibits less rapid variations at larger angles) and implausible (because observations of the PSF contain less signal at larger angles). Clearly some some sort of adaptive parametrization is required, which is finer near the core of the PSF and grows increasingly coarser moving outward.

Accordingly, we modify the method described above to allow arbitrary groupings of pixels on the pixel grid of the model image (and hence the PSF image) to be treated as single parameters. Specifically, we rewrite the normal equations to allow for (1) a pixellated parameter grid near the core of the PSF and (2) a circular annulus (if azimuthal symmetry is assumed) or annulus sector (if azimuthal symmetry is not assumed) parameter grid moving outward from the core. Together these modifications optimally represent the PSF over a huge dynamic range, vastly reduce the dimensionality of the problem, and remain linear in the parameters.

We emphasize that the method determines the PSF by *simultaneously* fitting all stars in the field, so there is no requirement of incorporating only isolated stars into the analysis.

In practice, we take locations and starting values of the energy fluxes of the stars from the Gaia DR3 catalog (Gaia Collaboration et al. 2017, 2018, 2021; Gaia Collaboration 2022), and we solve for the PSF image and the energy fluxes of the stars assuming a pixellated PSF at angular radius θ < 20 arcsec and an azimuthally-symmetric PSF at angular radius 20 arcsec $< \theta < 10$ arcmin, masking regions around galaxies and other non-stellar sources. We then subtract the model from the data, masking pixels of the result near the very cores of the stars at an isopohotal flux limit. (This masking is necessary because residuals near the cores of the stars can be large compared with the very low surface brightness limits farther from the cores.) A radial cut of a representative example of the PSF determined from the mosaic image is shown in Figure 11. It is apparent from Figure 11 that the "aureole" portion of the PSF (i.e. beyond an angular radius $\theta \approx 20$ arcsec) roughly follows a θ^{-2} radial profile, which is similar to the radial profiles of some other telescopes used for low-surfacebrightness imaging (e.g. Sandin 2014). The processed image of a portion of the mosaic image surrounding NGC 5907 obtained by modeling and subtracting the contributions of stars in the Gaia DR3 catalog is show in two different stretches in Figure 12; Figure 12 also shows schematic representation of features described in § 6 below.

Our analysis differs from the analysis of van Dokkum et al. (2019) in that we model and subtract only contributions from stars (and the occasional galaxy) that are contained in the Gaia DR3 catalog whereas they model and subtract contributions from all "compact emission sources." It is apparent from Figure 12 that our processed images exhibit a large number of faint sources, the vast majority of which are faint, background galaxies. But some fraction of these faint sources might be associated with NGC 5907, e.g. as dwarf galaxies, globular clusters, or perhaps other types of star clusters or associations. This difference between our analysis and the analysis of van Dokkum et al. (2019) leads to some important consequences, as is described below.

6 RESULTS AND COMPARISON WITH PREVIOUS WORK

Here we use the processed mosaic image of the region surrounding the galaxy NGC 5907 shown in Figure 12 to assess the various established, proposed, and tentative features reported by others and

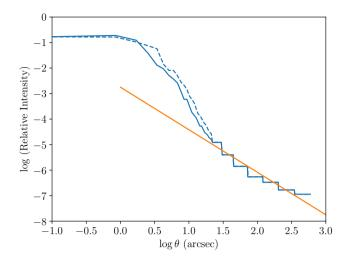


Figure 11. Radial cut of representative example of PSF determined according to description of § 4, normalized to unit area. Solid and dashed curves show PSF in two opposite directions. Orange line segment show θ^{-2} radial profile.

propose new features and new interpretations of some previously-reported features.

6.1 Eastern Stream

Our image of the eastern stream (which is indicated as feature 1 in green in Figure 12) through the luminance filter is consistent in location, size, shape, brightness, and overall morphology with the image of the eastern stream through the sum of the Sloan g' and r'filters presented by van Dokkum et al. (2019), which we established by overlaying and comparing the two images. In contrast, both our image and the image of van Dokkum et al. (2019) of the eastern stream are inconsistent with the image of the eastern stream through the sum of the R, G, B, and luminance filters presented by Martínez-Delgado et al. (2010) in the sense that the portion of the stream that is maximally displaced from the disk of the galaxy (i.e. the apex of the stream) in the image of Martínez-Delgado et al. (2010) lies interior to the same portion of the stream in our image and the image of van Dokkum et al. (2019), which we established by overlaying and comparing the three images. The displacement of the stream over this region between the two dichotomous sets of images amounts to ≈ 1 arcmin. This discrepancy in the location of the eastern stream was noted previously by van Dokkum et al. (2019).

We measured the typical surface brightness through the luminance filter of the eastern stream to be $\mu_{\text{lum}} \approx 27.4 \text{ mag arcsec}^{-2}$. This value may be compared with the peak surface brightness through the Sloan g' filter of the eastern stream measured by van Dokkum et al. (2019) to be $\mu_{g'} = 27.6 \text{ mag arcsec}^{-2}$.

6.2 Western Stream

Our image of the western stream (which is indicated as feature 2 in red in Figure 12) through the luminance filter is consistent in location, size, shape, brightness, and overall morphology with the image of the western stream through the Sloan g' and r' filters presented by van Dokkum et al. (2019), which we established by overlaying and comparing the two images. In contrast, both our image and the image of van Dokkum et al. (2019) of the western stream are inconsistent with the image of the western stream through the R,

G, B, and luminance filters presented by Martínez-Delgado et al. (2010) in the sense that the image presented by Martínez-Delgado et al. (2010) shows only a small portion of the western stream, near where it emerges from the southern edge of the galaxy, and does not show the remainder of the stream, as it bends toward the north, which we established by overlaying and comparing the three images. This discrepancy in the morphology of the western stream was noted previously by van Dokkum et al. (2019).

We measured the typical surface brightness through the luminance filter of the western stream to be $\mu_{lum}\approx 28.6$ mag $arcsec^{-2}$. This value may be compared with the typical surface brightness through the Sloan g' filter of the western stream measured by van Dokkum et al. (2019) to be $\mu_{g'}=28.8$ mag $arcsec^{-2}$. Thus, consistent with results of van Dokkum et al. (2019), we find that the western stream is of surface brightness significantly lower than that of the eastern stream (by ≈ 1.2 mag $arcsec^{-2}$). Apparently, images that fail to detect all or part of the western stream must not reach surface-brightness sensitivities of ≈ 28.7 mag $arcsec^{-2}$ over angular scales necessary to detect the stream.

Our image also shows an apparent gap in the western stream due east of the galaxy. The gap is followed by a marked thickening or enhancement of the western stream, although its surface brightness does not increase significantly in this thicker region. The apparent gap in the western stream is indicated as feature 2a in purple in Figure 12. The gap extends ≈ 70 arcsec, which at the distance of NGC 5907 corresponds to ≈ 6 kpc.

6.3 Putative Second Loop of Stellar Stream

Neither our image through the luminance filter nor the image through the Sloan g' and r' filters presented by van Dokkum et al. (2019) show any evidence at all of the second loop of the stellar stream seen in the image through the R, G, B, and luminance filters presented by Martínez-Delgado et al. (2010). The location of the putative second loop of the stellar stream is indicated as feature 3 in orange in Figure 12, which we determined by overlaying and tracing the feature from the image of Martínez-Delgado et al. (2010). Our image reaches a formal 3σ surface-brightness sensitivities over $10 \times 10 \text{ arcsec}^2$ regions of ≈ 29.9 mag arcsec⁻² (see Table 2), and van Dokkum et al. (2019) quote a 3σ surface-brightness sensitivity of 29.4 mag arcsec⁻² (although they do not state the angular scale over which this limit is meant to apply). We see no plausible way for color effects to explain the discrepancy, given that the observations reported by Martínez-Delgado et al. (2010) were obtained either through the luminance filter, as were our observations, or through a "synthetic" luminance filter (formed using observations obtained through the R, G, and B filters).

We conclude that the second loop of the stellar stream seen in the image presented by Martínez-Delgado et al. (2010) is not real and must result from some artifact of their data processing; we further suggest that the discrepancies in the location of the eastern stream and the morphology of the western stream must also result from some artifact of their data processing.

6.4 Putative Remnant of Nearly Disrupted Progenitor Galaxy and Luminosity-Weighted Midpoint of Eastern Stream

Our image shows a "feature" (which is indicated as feature 4a in white in Figure 12) near the location of the "density enhancement near the luminosity-weighted midpoint of the [eastern] stream" noted by van Dokkum et al. (2019). But our images resolve this feature into

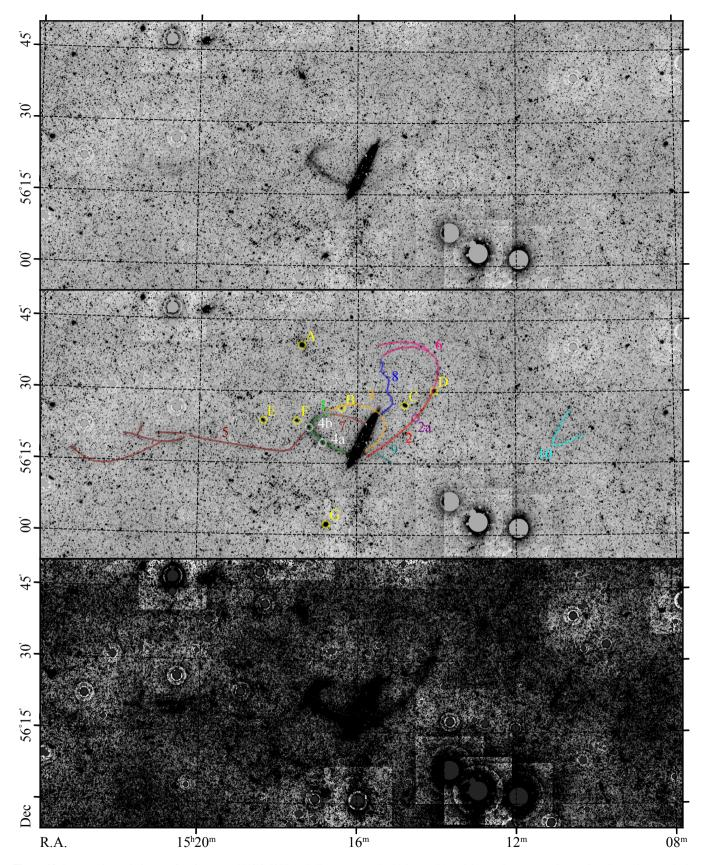


Figure 12. Processed mosaic image of region around NGC 5907 at shallower (top and middle panels) and deeper (bottom panel) stretches. Image is smoothed by Gaussian kernel of FWHM = 2.5 pix. Middle panel shows schematic representation of features described in § 6 labeled as follows: 1 (green) eastern stream, 2 (red) western stream, 2a (purple) apparent gap in western stream, 3 (orange) putative second loop of stellar stream, 4a and 4b (white) feature and clump of sources in eastern stream, 5 (maroon) linear feature terminating on patch, 6 (pink) putative extension of western stream, 7 (brown) continuation of eastern stream, 8 (blue) western "horn", 9 (turquoise) southern "spur," 10 (aqua) western "hook," and A–G (yellow) dwarf galaxies.

a clump of sources, which we interpret as members of a background galaxy group or cluster rather than as the "likely remnant of a nearly disrupted progenitor galaxy" proposed by van Dokkum et al. (2019).

Our image also shows a different clump of sources (which is indicated as feature 4b in white in Figure 12) near the "luminosityweighted midpoint" of the eastern stream, including one relatively bright galaxy that might be a dwarf galaxy associated with NGC 5907 or might be a member of a background galaxy group or cluster. (This galaxy is included into the Gaia DR3 catalog, and our analysis described in § 4 attempted to model and subtract it, although unsuccessfully since it is not a point source.) But in either case, it is clear from Figure 12 that galaxies (background or otherwise) or other discrete sources contribute significantly to the luminosity-weighted midpoint of the eastern stream. In particular, much of the "density enhancement" of the eastern stream found by van Dokkum et al. (2019) (i.e. the portions of their Figure 3 depicted in red) is in fact contributed by discrete sources, which we established by overlaying and comparing our Figure 12 with their Figure 3. (The discrete sources can be picked out one by one by means of this comparison.) Further, the possible asymmetry in the density enhancement of the eastern stream noted by van Dokkum et al. (2019) is in fact contributed by discrete sources, including in particular the relatively bright galaxy noted above.

We conclude that the feature proposed by van Dokkum et al. (2019) as the likely remnant of a nearly disrupted progenitor galaxy is not the progenitor galaxy but is in fact a member of a background galaxy group or cluster and that the density enhancement and possible asymmetry of the density enhancement of the eastern stream noted by van Dokkum et al. (2019) is in fact contributed by discrete sources. This difference of interpretation presumably arises due to the higher angular resolution of our observations in comparison with the observations of van Dokkum et al. (2019).

6.5 Linear Feature Terminating on Patch

Our images confirm the "linear" feature emanating from the eastern stream toward the east and terminating on a "patch" of emission identified by van Dokkum et al. (2019). But our images further indicate that the feature continues past the patch toward the east and eventually terminates on another patch of emission located ≈ 0.37 deg away from the first patch (which itself is located ≈ 0.67 deg from the center of NGC 5907). Our images also further indicate that first patch is itself resolved into two roughly parallel linear segments running roughly east-west and another clump of emission toward the east. This entire structure is indicated as feature 5 in maroon in Figure 12. In total, the structure stretches ≈ 0.85 deg from where it emanates near the apex of the eastern stream to where it terminates on the second patch.

We measured the typical surface brightness through the luminance filter of the first patch to be $\mu_{lum}\approx 28.1$ mag arcsec $^{-2}$ and the typical surface brightness through the luminance filter of the second patch to be $\mu_{lum}\approx 28.9$ mag arcsec $^{-2}$. Thus we find that both patches are of surface brightness significantly lower than that of the eastern stream and that the first patch is of surface brightness significantly higher than that of the western stream while the second patch is of surface brightness comparable to that of the western stream. The linear feature and the continuation of the linear feature vary significantly in brightness along their lengths, but we measured a typical surface brightness through the luminance filter of these features to be $\mu_{lum}\approx 29.7$ mag arcsec $^{-2}$. Thus we find that the linear feature and the continuation of the linear feature are typically of surface brightness significantly lower than that of the patches (by

 ≈ 1.0 mag arcsec⁻²), although we note a significant brightening of the linear feature west of the first patch, roughly midway between the first patch and the eastern stream. We measured the angular extent of the first patch to be $\approx 530 \times 240$ arcsec² and the angular extent of the second patch to be $\approx 220 \times 270$ arcsec², where the measurements apply to an isophotal contour of ≈ 29 mag arcsec⁻².

We conclude that the linear feature emanating from the eastern stream toward the east and terminating on a patch identified by van Dokkum et al. (2019) are part of a yet larger structure. If this structure is at the distance of NGC 5907 (which is plausible or likely given that it appears to emanate near the apex of the eastern stream), then the first patch is located ≈ 200 kpc from the center of the galaxy, the second patch is located ≈ 300 kpc from the center of the galaxy, and the entire structure stretches ≈ 240 kpc from where it emanates near the apex of the eastern stream to where it terminates on the second patch. Further, the spatial extent of the first patch is $\approx 43 \times 20 \text{ kpc}^2$, the spatial extent of the second patch is $\approx 18 \times 22 \text{ kpc}^2$, the absolute magnitude through the luminance filter of the first patch is ≈ -15.4 , i.e. roughly 0.6% that of the Milky Way, and the absolute magnitude through the luminance filter of the second patch is ≈ -14.2 , i.e. roughly 0.2% that of the Milky Way (where we take the Sloan g' absolute magnitude of the Milky Way to be -21.0, e.g. Bland-Hawthorn & Gerhard 2016). Multi-band imaging of the field surrounding NGC 5907 will be necessary to establish the nature of the patches of emission.

6.6 Putative Extension of Western Stream

Our image confirms the extension of the western stream (which is indicated as feature 6 in pink in Figure 12) tentatively identified by van Dokkum et al. (2019). This extension continues along the direction of the western stream described in § 6.2 toward the north and then curls back south toward NGC 5907, about 0.3 deg north of the center of the galaxy. Our image further shows that the stream appears to bifurcate near its apex. We measured the typical surface brightness through the luminance filter of the extension of the western stream to be $\mu_{\text{lum}} \approx 28.9 \text{ mag arcsec}^{-2}$. Thus we find that the extension of the western stream is of surface brightness lower than that of the rest of the western stream (by $\approx 0.3 \text{ mag arcsec}^{-2}$).

6.7 Putative Continuation of Eastern Stream

Our image confirms the continuation of the eastern stream (which is indicated as feature 7 in brown in Figure 12) tentatively identified by van Dokkum et al. (2019). We measured the typical surface brightness through the luminance filter of the continuation of the eastern stream to be $\mu_{\text{lum}} \approx 29.0$ mag arcsec⁻². Thus we find that the continuation of the eastern stream is of surface brightness significantly lower than that of the bulk of the eastern stream and lower even than that of the western stream. There is some indication of a gap between the brighter bulk of the eastern stream and the fainter continuation of the eastern stream that joins up to the disk, although this gap is roughly coincident with three Gaia sources, which muddy the interpretation.

6.8 Western "Horn"

Our image reveals a new western "horn" (which is indicated as feature 8 in blue in Figure 12) emanating from the western side of the northern portion of the disk of NGC 5907 and extending to the northwest. The horn constitutes a thin, roughly linear feature of diffuse emission. We also tentatively identify a continuation of the

horn that meanders from the northern tip of the horn northward by ≈ 0.15 deg to the extension of the western stream described in § 6.6. We measured the typical surface brightness through the luminance filter μ_{lum} of the western horn to be $\mu_{lum} \approx 29.0$ mag arcsec⁻². Thus we find that the western horn is of surface brightness lower than that of the western stream.

The western horn is apparent in the image through the sum of the Sloan g' and r' filters presented by van Dokkum et al. (2019), although these authors did not call attention to the feature.

6.9 Southern "Spur"

Our image reveals a new southern "spur" emanating from the southern portion of the western stream and continuing to the southwest. The spur comprises a band of diffuse emission of thickness comparable to the thickness of the western stream that runs almost perpendicular to the western stream. We measured the typical surface brightness through the luminance filter μ_{lum} of the southern spur to be $\mu_{lum} \approx 29.0$ mag arcsec⁻². Thus we find that the southern spur is of surface brightness lower than that of the western stream.

The southern spur is not obviously evident in the image through the sum of the Sloan g' and r' filters presented by van Dokkum et al. (2019).

6.10 Western "Hook"

Our image reveals a new western "hook" (which is indicated as feature 10 in aqua in Figure 12) located ≈ 0.68 deg due west of the center of NGC 5907. Hence the western hook is about as far west of the galaxy as the first patch described in § 6.5 is east of the galaxy. There is no clear and obvious connection between the hook and NGC 5907, but if the hook is at the distance of the galaxy, then it is located ≈ 200 kpc from the center of the galaxy. We measured the typical surface brightness through the luminance filter μ_{lum} of the western hook to be $\mu_{lum} \approx 29.0$ mag arcsec⁻². Thus we find that the western hook is of surface brightness lower than that of the western stream.

The western hook is not covered by the image through the sum of the Sloan g' and r' filters presented by van Dokkum et al. (2019).

6.11 Dwarf Galaxies

Figure 12 calls attention to several sources, which are identified as sources A through G in yellow in the figure. Source B in Figure 12 is the previously-uncataloged putative dwarf galaxy located just west of the eastern stream reported by van Dokkum et al. (2019). The proximity of this galaxy to the eastern stream obviously suggests that the galaxy is associated with (rather than behind) NGC 5907, but without spectroscopy or multi-band imaging, it is not possible to know for sure.

But interestingly, there are several *known* galaxies in the immediate vicinity of NGC 5907—two of which are *known* to be associated with the galaxy—that were not considered by the analysis of van Dokkum et al. (2019) because they were modeled and subtracted by their analysis as "compact emission sources." These include sources A, C, D, E, and G in Figure 12. In particular:

• Source A: This galaxy (MCG+10-22-010) exhibits a heliocentric recession velocity $781 \pm 80 \text{ km s}^{-1}$ (Falco et al. 1999) consistent with the recession velocity of NGC 5907 and a Sloan g' magnitude $g' = 14.987 \pm 0.003$ (Adelman-McCarthy & et al. 2011) and is morphologically classified as a dwarf irregular galaxy (Ann et al. 2015). At the distance of NGC 5907, the absolute magnitude of

source A is ≈ -16.2 , i.e. roughly comparable to that of the SMC. The projected impact parameter of source A to the center of NGC 5907 is ≈ 117 kpc and to the plane of the disk is ≈ 99 kpc.

- Source C: This galaxy (LEDA 54419) exhibits a heliocentric recession velocity 710 km s $^{-1}$ (Wenger et al. 2000) consistent with the recession velocity of NGC 5907 and a Sloan g' magnitude $g'=16.206\pm0.004$ (Wenger et al. 2000) and is morphologically classified as a Magellanic irregular galaxy (Ann et al. 2015). At the distance of NGC 5907, the absolute magnitude of source C is ≈-14.9 , i.e. roughly 0.3 times that of the SMC. The projected impact parameter of source C to the center of NGC 5907 is ≈56 kpc and to the plane of the disk is ≈21 kpc.
- Source D: This galaxy (2MASX J15140431+5630186) exhibits a Gaia G magnitude $G=19.615\pm0.008$ (Gaia Collaboration 2022). If it is at the distance of NGC 5907, then the absolute magnitude of source D is ≈ -11.5 , i.e. roughly 1% that of the SMC, and the projected impact parameter to the center of NGC 5907 is ≈ 89 kpc and to the plane of the disk is ≈ 43 kpc. This galaxy is of particular interest because it is located at the very terminus of the western stream (and at the starting point of the putative extension of the western stream), near the location of the thickening or enhancement of the western stream noted in § 5.2. Because the galaxy is included into the Gaia DR3 catalog, our analysis described in § 4 attempted (unsuccessfully, because it is not a point source) to model and subtract it.
- Source E: This galaxy (LEDA 2535522) exhibits a Gaia G magnitude $G = 20.44 \pm 0.01$ (Gaia Collaboration 2022). If it is at the distance of NGC 5907, then the absolute magnitude of source E is ≈ -10.7 , i.e. roughly 0.6% that of the SMC, and the projected impact parameter to the center of NGC 5907 is ≈ 106 kpc and to the plane of the disk is ≈ 102 kpc. As with source D, this galaxy is included into the Gaia DR3 catalog, and our analysis attempted to model and subtract it.
- Source G: This galaxy (LEDA 2523331) exhibits a Gaia G magnitude G=20.58 (Gaia Collaboration 2022). If it is at the distance of NGC 5907, then the absolute magnitude of source G is ≈ -10.6 , i.e. roughly 0.5% that of the SMC, and the projected impact parameter to the center of NGC 5907 is ≈ 96 kpc, and it is roughly in the plane of the disk. As with source D, this galaxy is included into the Gaia DR3 catalog, and our analysis attempted to model and subtract it.

Properties of these galaxies are summarized in Table 3, which for each galaxy lists the source, name, ICRS coordinates, heliocentric recession velocity $v_{\rm rec}$, Sloan g' or Gaia G magnitude, morphological type, absolute Sloan g' or Gaia G magnitude M, impact parameter b, and impact parameter to the plane of the disk $b_{\rm disk}$.

Source F in Figure 12 might appear at first glance to be a dwarf galaxy in close proximity to the eastern stream. But our images resolve this "source" into a number discrete sources, which we interpret as a background galaxy group or cluster. There are several other background galaxy groups or clusters also evident in the images.

We conclude that there are at least several (and possibly many more) dwarf galaxies associated with NGC 5907 that may play roles as progenitor galaxies. The few galaxies considered here are far from a complete inventory of dwarf galaxies and possible dwarf galaxies associated with NGC 5907, and as is discussed in § 4, our processed images exhibit a large number of faint sources, some fraction of which could be dwarf galaxies. Multi-object spectroscopy or multi-band imaging of faint sources in the field surrounding NGC 5907 will be necessary to identify other dwarf galaxies associated with NGC 5907.

Table 3. Properties of known galaxies in the immediate vicinity of NGC 5907.

		J2000		$v_{\rm rec}$			Absolute	b	$b_{ m disk}$
Source	Name	R.A.	Dec	(km s^{-1})	Type	Magnitude	Magnitude	(kpc)	(kpc)
Α	MCG+10-22-010	15:17:25.2	+56:39:48.5	781 ± 80	dIrr	14.987 ± 0.003	-16.2	117	99
C	LEDA 54419	15:14:47.8	+56:27:14.8	710	dIrr	16.2006 ± 0.004	-14.9	56	21
D	2MASX J15140431+5630186	15:14:04.3	+56:30:18.7			19.6156 ± 0.008	-11.5 (?)	89	43
E	LEDA 2535522	15:18:23.6	+56:23:58.1			20.44 ± 0.01	-10.7(?)	106	102
G	LEDA 2523331	15:16:46.5	+56:02:16.0			20.58	-10.6 (?)	86	0

6.12 Possible Confusion with Galactic Cirrus

To assess possible confusion with Galactic cirrus in the direction of NGC 5907, we examined (1) AKARI far-infrared all-sky survey maps at 65, 90, 140, and 165 μ m (Doi et al. 2015) and (2) an interstellar reddening map derived from H I emission (Lenz et al. 2017). We found that at the Galactic coordinates l = 91.58 deg and b = +51.09deg of the galaxy, there is negligible infrared emission at any AKARI bandpass, and there is negligible interstellar reddening. We therefore consider it highly unlikely that any of the very low-surface-brightness features in the direction of the galaxy arise due to Galactic cirrus.

7 SUMMARY AND DISCUSSION

The results described in § 5 confirm the overall picture of the galaxy NGC 5907 and its stellar stream advanced by van Dokkum et al. (2019): the stellar stream consists of a single curved structure that stretches 220 kpc from the brighter eastern stream, across the southern edge of the galaxy, to a fainter western stream that bends to the north and then curls back south toward the galaxy. But these results also demonstrate that the situation is more subtle and complex in several respects: (1) the western stream appears to bifurcate near its apex, (2) there is an apparent gap of ≈ 6 kpc in the western stream due east of the galaxy, (3) there is no evidence of the remnant of a progenitor galaxy within the eastern stream, although (4) there are many other possible progenitor galaxies, including some that are quite close and at least one that is located within the western stream, (5) there is another structure that stretches 240 kpc and that contains two very large, very low-surface-brightness patches of emission, one of which was noted by van Dokkum et al. (2019) and another of which was not, and (6) there are other notable new features, including a western "horn," a southern "spur," and a western "hook."

We consider several aspects of these results to be particularly significant as follows:

First, we note that two different N-body simulations (i.e. by Martínez-Delgado et al. 2010 and by van Dokkum et al. 2019) predict two very different configurations for the stellar stream, both of which apparently run counter to observation (in one case with respect to the second loop and in the other case with respect to the remnant of a nearly disrupted progenitor galaxy). This suggests to us that the boundary conditions of both simulations are very significantly under constrained. We propose that a correct and complete understanding of the nature and origin of the stellar stream can be obtained using N-body simulations only if additional boundary conditions can be supplied, most crucially relating to the eastern stream and of source

Second, we are intrigued by the number and variety of stellar streams in the vicinity of NGC 5907, including the eastern stream, the western stream, the structure containing the linear feature and two patches of emission, and possibly the western hook. Given that more than 100 stellar streams are known in the vicinity of the Milky Way (e.g. Mateu 2022), there is every reason to suspect that similar networks of stellar streams might be found around other galaxies, including NGC 5907.

Third, we are struck by the apparent gap in the western stream. Gaps in stellar streams may be caused by the impacts of dark "subhalos" or satellites orbiting within the halos of massive galaxies (e.g. Helmi & Koppelman 2016; Koppelman & Helmi 2020). Hence the apparent gap in the western stream may be indicative of a dark subhalo or satellite in the vicinity of the galaxy. Further observations and analysis are clearly required to confirm and interpret the apparent gap.

Finally, we are puzzled by the nature of the two very large, very low-surface-brightness patches of emission. If these patches are considered to be galaxies, then they are extremely low-surfacebrightness galaxies; if these patches are not considered to be galaxies, then is not clear what they are, and they presumably represent some new phenomenon with no known analog. We speculate that the presence of the patches is in some way related to the presence of the tidal stream, although the morphology of the linear feature and the patches together is vaguely reminiscent of "jellyfish" galaxies (e.g. Moretti et al. 2018) or of the young, isolated stellar systems found in the Virgo cluster (Jones et al. 2022), both of which may be formed via ram-pressure stripping of gas from a parent galaxy.

There is clearly more to be learned about the galaxy NGC 5907 and its stellar streams, and we anticipate using Condor to obtain additional deep observations of NGC 5907 and the NGC 5866 Group through its complement of broad- and narrow-band filters.

ACKNOWLEDGMENTS

This material is based upon work supported by the National Science Foundation under Grants 1910001, 2107954, and 2108234. We gratefully acknowledge Chris Mihos and an anonymous referee for very valuable comments on earlier drafts of the manuscript; the staff of Dark Sky New Mexico, including Diana Hensley, Michael Hensley, and the late Dennis Recla for their outstanding logistical and technical support; and Yuri Petrunin for crafting six superb instruments. This work made use of the following software: astroalign (Beroiz et al. 2020), astropy (Astropy Collaboration et al. 2013, 2018), django (Django Software Foundation 2019), Docker (Merkel 2014), DrizzlePac (Gonzaga et al. 2012), NoiseChisel (Akhlaghi & Ichikawa 2015; Akhlaghi 2019), numba (Lam et al. 2015), numpy (Harris et al. 2020), photutils (Bradley et al. 2020), scipy (Virtanen et al. 2020), SExtractor (Bertin & Arnouts 1996).

DATA AVAILABILITY

All raw Condor data are available following an 18-month proprietary period. All raw and processed data described here, including the coadded images of Figures 1 through 6 and the mosaic image of Figure 7, are available on the Condor web site https://condorarraytelescope.org/data_access/ or by contacting the corresponding author.

REFERENCES

```
Abraham R. G., van Dokkum P. G., 2014, PASP, 126, 55
Adelman-McCarthy J. K., et al. 2011, VizieR Online Data Catalog, p. II/306
Akhlaghi M., 2019, arXiv e-prints, p. arXiv:1909.11230
Akhlaghi M., Ichikawa T., 2015, ApJS, 220, 1
Ann H. B., Seo M., Ha D. K., 2015, ApJS, 217, 27
Astropy Collaboration et al., 2013, A&A, 558, A33
Astropy Collaboration et al., 2018, AJ, 156, 123
Beroiz M., Cabral J., Sanchez B., 2020, Astronomy and Computing, 32,
    100384
Bertin E., Arnouts S., 1996, A&AS, 117, 393
Bland-Hawthorn J., Gerhard O., 2016, ARA&A, 54, 529
                                  2020,
                                             astropy/photutils:
                                                                  1.0.0,
   doi:10.5281/zenodo.4044744, https://doi.org/10.5281/zenodo.
    4044744
Byun W., et al., 2022, PASP, 134, 084101
Chao C. Y.-P., et al., 2019, Sensors, 19
Django Software Foundation 2019, Django, https://djangoproject.com
Doi Y., et al., 2015, PASJ, 67, 50
Falco E. E., et al., 1999, PASP, 111, 438
Gaia Collaboration 2022, VizieR Online Data Catalog, p. I/355
Gaia Collaboration et al., 2017, A&A, 605, A79
Gaia Collaboration et al., 2018, A&A, 616, A1
Gaia Collaboration et al., 2021, A&A, 649, A1
Gonzaga S., Hack W., Fruchter A., Mack J. e., 2012, The DrizzlePac
    Handbook. STScI, Baltimore, MD
Harris C. R., et al., 2020, Nature, 585, 357
Helmi A., Koppelman H. H., 2016, ApJ, 828, L10
Herschel W., 1789, Philosophical Transactions of the Royal Society of
   London, 79, 212
Jones M. G., et al., 2022, ApJ, 935, 51
Koppelman H. H., Helmi A., 2020, arXiv e-prints, p. arXiv:2011.11684
Laine S., et al., 2016, AJ, 152, 72
Lam S. K., Pitrou A., Seibert S., 2015, in Proceedings of the Second Workshop
    on the LLVM Compiler Infrastructure in HPC. pp 1-6
Lanzetta K. M., Gromoll S., Shara M. M., Berg S., Valls-Gabaud D., Walter
    F. M., Webb J. K., 2023, PASP, 135, 015002
Lenz D., Hensley B. S., Doré O., 2017, ApJ, 846, 38
Martínez-Delgado D., et al., 2010, AJ, 140, 962
Mateu C., 2022, arXiv e-prints, p. arXiv:2204.10326
Merkel D., 2014, Linux journal, 2014, 2
Moretti A., et al., 2018, MNRAS, 480, 2508
Müller O., Vudragović A., Bílek M., 2019, A&A, 632, L13
Paillassa M., Bertin E., Bouy H., 2020, A&A, 634, A48
Press W. H., Teukolsky S. A., Vetterling W. T., Flannery B. P., 2007,
   Numerical Recipes 3rd Edition: The Art of Scientific Computing,
       edn. Cambridge University Press, http://www.amazon.
    com/Numerical-Recipes-3rd-Scientific-Computing/dp/
   0521880688/ref=sr_1_1?ie=UTF8&s=books&qid=1280322496&
Sackett P. D., Morrisoni H. L., Harding P., Boroson T. A., 1994, Nature, 370,
   441
Sancisi R., 1976, A&A, 53, 159
Sandin C., 2014, A&A, 567, A97
Sasaki T., 1987, PASJ, 39, 849
```

Shang Z., et al., 1998, ApJ, 504, L23

```
Springob C. M., Haynes M. P., Giovanelli R., Kent B. R., 2005, ApJS, 160, 149
Tully R. B., Courtois H. M., Sorce J. G., 2016, AJ, 152, 50
Virtanen P., et al., 2020, Nature Methods, 17, 261
Wenger M., et al., 2000, A&AS, 143, 9
Zheng Z., et al., 1999, AJ, 117, 2757
van Dokkum P., et al., 2019, ApJ, 883, L32
van der Kruit P. C., 1979, A&AS, 38, 15
```

This paper has been typeset from a TFX/IATFX file prepared by the author.